Noise propagation and MP-PCA image denoising for high-resolution quantitative R_2^* , T_2^* , and magnetic susceptibility mapping (QSM)

Liad Doniza, Mitchel Lee, Tamar Blumenfeld-Katzir, Moran Artzi, Dafna Ben-Bashat, Orna Aizenstein, Dvir Radunsky, Fenella Kirkham, George Thomas, Rimona S. Weil, Karin Shmueli, Noam Ben-Eliezer

Abstract— Objective: Quantitative Susceptibility Mapping (QSM) measures magnetic susceptibility of tissues, aiding in the detection of pathologies like traumatic brain injury, cerebral microbleeds, Parkinson's disease, and multiple sclerosis, through analysis of variations in substances such as iron and calcium. Despite its clinical value, using high-resolution QSM (voxel sizes < 1 mm³) reduces signal-to-noise ratio (SNR), which compromises diagnostic quality. Methods: Denoising of T2*-weighted (T2*w) data was implemented using Marchenko-Pastur Principal Component Analysis (MP-PCA), allowing to enhance the quality of R2*, T2*, and QSM maps. Proof of concept of the denoising technique was demonstrated on a numerical phantom, healthy subjects, and patients with brain metastases and sickle cell anemia. Results: Effective and robust denoising was observed across different scan settings, offering higher SNR and improved accuracy. Noise propagation was analyzed between T2*w, R2*, and T2* values, revealing augmentation of noise in T2*w compared to R2* values. Conclusions: The use of MP-PCA denoising allows the collection of high resolution (~0.5 mm³) QSM data at clinical scan times, without compromising SNR. Significance: The presented pipeline could enhance the diagnosis of various neurological diseases by providing higher-definition mapping of small vessels and of variations in iron or calcium.

Code available at:

[https://github.com/NoamBenEliezer/T2-w-MP-PCA].

Index Terms— Denoising, magnetic susceptibility, principal component analysis, quantitative susceptibility mapping, QSM, signal to noise ratio, T₂*, R₂*.

Manuscript received 19 August 2024; Karin Shmueli was supported by European Research Council Consolidator Grant DiSCo MRI SFN 770939. Mitchel Lee was supported by the Engineering and Physical Sciences Research Council (EPSRC) funded UCL Centre for Doctoral Training in Intelligent, Integrated Imaging in Healthcare (i4health) (EP/S021930/1).

L. Doniza is with the School of Electrical Engineering, Tel Aviv University (TAU), Tel Aviv, Israel. M. Lee, and K. Shmueli are with the UCL Department of Medical Physics & Biomedical Engineering, University College London, London, UK. Blumenfeld-Katzir, D. Radunsky, and N. Ben-Eliezer are with the Biomedical Engineering Department, TAU, Tel-Aviv, Israel. N. Ben-Eliezer is also with Sagol School of Neuroscience, TAU, Tel-Aviv, Israel, and The Center for Advanced Imaging Innovation and Research (CAI2R), Langone Medical Center, New York University, New York, NY, USA (e-mail: noambe@tauex.tau.ac.il). F Kirkham is with the Developmental Neurosciences Department, UCL Great Ormond Street Institute of Child Health, University College London, London, UK. George Thomas and Rimona S. Weil are with the UCL Dementia Research Centre, University College London, London, UK. M. Artzi, and D. Ben Bashat are also with Sagol Brain Institute, Tel Aviv Sourasky Medical Center, Tel Aviv, Israel, and with Sagol School of Neuroscience, TAU, Tel-Aviv, Israel. O. Aizenstein is also with Imaging Division, Tel Aviv Sourasky Medical Center, Tel-Aviv, Israel.

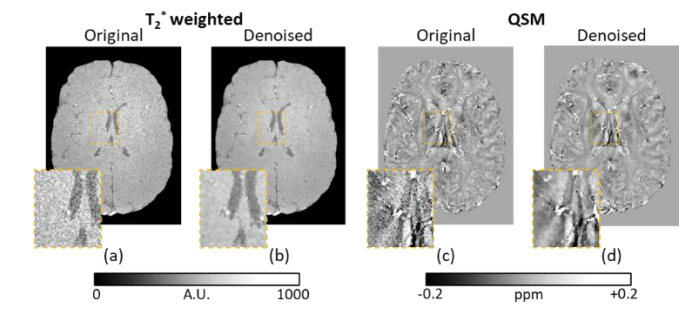


Fig. 1. Original and denoised T_2^* images along with their corresponding quantitative susceptibility maps $(0.5^3$ isotropic millimeter resolution). (a) shows the original magnitude image, (b) presents the denoised image, and (c-d) displays their respective QSM maps. A zoomed-in region of each image is shown at the bottom left corner.

I. INTRODUCTION

A. Motivation for high-resolution QSM

Quantitative susceptibility mapping (QSM) [1]-[4] is a common MRI technique for measuring the magnetic susceptibility of tissues (χ) . QSM is mainly utilized for detecting pathologies that involve dysregulations in iron, calcium, and myelin content, and has been utilized as a biomarker for microbleeds in traumatic brain injury, sickle cell anemia, brain metastases, glioma, multiple sclerosis, and Parkinson's disease [2], [5]–[11]. Several studies have shown that increasing the spatial resolution of clinical data lowers partial volume effects and offers more faithful mapping of QSM values, particularly in small structures [2], [11]-[13]. Specifically, high-resolution susceptibility maps important for separating subthalamic nuclei, characterization of the internal structure of the substantia nigra, which plays a central role in Parkinson's disease and in planning deep brain stimulation surgeries [14]-[16]. Additionally, QSM is useful for detecting increased susceptibility in the basal ganglia [17] as well as paramagnetic rims of iron-laden active microglia and macrophages in multiple sclerosis (MS) lesions, correlating with cognitive function and with the expanded disability status scale (EDSS) [18], [19]. Collecting high resolution data, however, comes with a tradeoff of lower SNR, and reduced diagnostic quality [12], [13].

Typically, QSM values are reconstructed from complex T_2^* -weighted (T_2^*w) images, acquired using a 3D multi gradient echo (GRE) protocol. As QSM involves solving the field-to-source inverse problem, noise amplification is a major issue and can lead to streaking artifacts and quantification errors [20]. Further, due to the intricate QSM reconstruction pipeline [21] and the use of complex data, noise propagation affects QSM values beyond simple

reduction in SNR [22], [23] and may lead to artifacts relating to inaccurate phase unwrapping [2], [11]. Solutions to these problems are typically based on adding regularizations or adjusting hyperparameters and weighting terms in the QSM processing pipeline [24], [25]. Other applications that could benefit from denoising QSM data are quantifying microvascular oxygen extraction fraction (**OEF**) based on the QSM-OEF technique [26], and fast QSM acquisition methods such as echo planer imaging (**EPI**) based QSM [27], [28].

B. Denoising QSM - Previous work

An effective approach to avoid noise-related artifacts and produce high-resolution QSM maps is to denoise the raw complex T_2^*w data that are used as input to the QSM pipeline. Bazin *et al.* [29], for example, introduced a technique that employs Principal Component Analysis (**PCA**) to denoise magnetization-prepared gradient echo (**MPRAGE**) data, for QSM processing at 7T. Zhang *et al.* [30] utilized a self-supervised deep neural network for denoising EPI data from multiple slices and echo-times. This model, however, is designed to denoise only the magnitude, rather than complex images, and may therefore produce less optimal results for QSM which relies heavily on the phase information.

Some QSM reconstruction approaches use supervised and unsupervised deep learning which simplify the QSM pipeline and introduce some level of denoising, e.g., Plug-and-Play QSM [31], DeepQSM [32], QSMnet [33], MoDIP [34], or AFTER [35]. These methods, however, still operate on the main field inhomogeneity map generated from noisy data, potentially affecting the QSM results, and may thus also benefit from a priori denoising of the raw T_2^*w data. Notwithstanding promising results of recent techniques [31], [35], deep learning approaches may encounter limitations in terms of generalization, seeing as supervised networks require large and diverse training sets, including variations in susceptibility values and, ideally, varied resolutions, in order to function effectively, while a lack of such diverse data can lead to suboptimal results [33], [36]–[38].

C. Existing applications of MP-PCA denoising

Recent studies have demonstrated the utility of Marchenko-Pastur (MP) criteria in PCA for effective noise reduction. This method relies on the fact that, for MRI signals, the eigenvalues of noise obey the universal MP law of random matrix theory [39]. Its applications have been explored in several MRI modalities, including Diffusion-weighted MRI [40], enhancement of parameter estimation in multiexponential relaxometry [41], production of more precise T_2 maps [42], multi-parametric quantitative MRI of the spinal cord [43], language mapping in functional MRI for patients with brain tumors [44], and diffusion-weighted spectroscopy [45].

In this work, MP-PCA was employed for denoising multi-GRE data, which is both commonly utilized and the recommended approach for accurate QSM [21], [23]. MP-PCA was integrated as an initial step in processing complex T_2^*w brain images within the QSM pipeline [46] (Fig. 1). Denoising efficiency was also evaluated on T_2^*w magnitude images, and on R_2^* , T_2^* , and QSM maps. Successful proof of concept is shown on a numerical phantom and *in vivo* brain

data in healthy individuals as well as patients with sickle cell anemia, brain metastases, and Parkinson's disease. These applications were conducted across a range of scan settings and spatial resolutions, highlighting the method's robustness.

II. THEORY

A. Theory of MP-PCA denoising

This Section contains a concise overview of MP-PCA denoising theory applied to T_2^*w imaging. More comprehensive descriptions can be found in [40]–[42]. Multiecho T_2^*w magnitude and phase data were acquired using a 3D GRE sequence. We denote the acquired 4D complex data matrix as $D \in \mathbb{C}^{[N_\chi,N_y,N_z,N_E]}$, where three dimensions represent the spatial domain, and the fourth denotes the number of echoes N_E. A sliding 4D window denoted as $W \in$ $\mathbb{C}^{[n_x,n_y,n_z,N_E]}$ is used to traverse the entire dataset D, while denoising is applied within that window. A natural choice for a dataset with isotropic resolution is a 3D isotropic window size of $N_W \times N_W \times N_W$. The matrix W surrounding each voxel is vectorized to $N_V = N_W^3$, resulting in a 2D matrix $A \in$ $\mathbb{C}^{N_V \times N_E}$. A is then normalized to \hat{A} by subtracting the mean signal within each 3D spatial window $\bar{A} \in \mathbb{C}^{1 \times N_E}$ for each echo time (TE) according to:

$$\hat{A}(i) = A(i) - \bar{A}(i) \cdot 1_{N_V \times 1} \quad \forall i \in 1 \dots N_E$$

 \hat{A} is then decomposed into its linearly independent sources, or principal components (PCs), using singular value decomposition (SVD) [47]

$$SVD(\hat{A}) = U\Lambda V^T \tag{2}$$

The $M = \min(N_V, N_E)$ diagonal elements of Λ represent the singular values of \hat{A} , and Λ^2 is an $M \times M$ diagonal matrix containing the eigenvalues $\lambda_1 \dots \lambda_M$. Assuming that noise has a Marchenko-Pastur distribution, the first P eigenvalues of \hat{A} can be associated with the signal, whereas the remaining (M - P) elements represent noise [39]–[41]. The value of P is determined by the minimum value that obeys the following inequality [40]:

$$\frac{\sum_{i=P+1}^{M} \lambda_i}{M-P} > \frac{\lambda_{P+1} - \lambda_M}{4\sqrt{\frac{M-P}{N_V}}}$$
(3)

Consequently, noise is removed by truncating the last $\lambda_{P+1} \dots \lambda_M$ eigenvalues and transforming back to the spatial domain using:

$$\hat{A}' = U \Lambda' V^T \tag{4}$$

Finally, the mean value at each time point \bar{A} is added back to \hat{A}' . This process iterates across the entire spatial domain, moving W one voxel at a time. The denoised signal at each voxel is then given by the average value from all windows that include that voxel [48].

B. Quantitative mapping of magnetic susceptibility

QSMs were computed from magnitude and phase images. Phase images reflect the magnetic field inhomogeneities, $\Delta B_0(\vec{r})$ which, in turn, represent a convolution of the tissue susceptibility $\chi(\vec{r})$ with the dipole field distribution $d(\vec{r})$ [2]:

$$\Delta B_0(\vec{r}) = B_0 \cdot \{ \chi(\vec{r}) * d(\vec{r}) \} \tag{5}$$

This equation is known as the forward model, where B_0 is the static homogeneous magnetic field in the z-direction, and the unit dipole $d(\vec{r})$ is defined as:

$$d(\vec{r}) = \frac{3\cos^2 \varphi - 1}{4\pi \vec{r}^3}$$
 (6)

where φ is the angle between the position vector \vec{r} and the main magnetic field (B_0) direction (\hat{z}) .

Several pipelines exist for reconstructing QSMs. Here, we used the pipeline described by Karsa *et al.* [46] which conforms to the recent consensus recommendations [21]. The process begins with non-linear fitting of the complex data over echo times [49]–[52] to calculate the total field map $\Delta B_0(\vec{r})$ and a noise weighting matrix W_N . This is followed by Laplacian phase unwrapping [52], [53]. Subsequently background field is removed by generating a brain mask using FSL's Brain Extraction Tool (**BET**) [54], combined with a mask based on thresholding W_N at its mean. Projection onto Dipole Fields (**PDF**) [55] is then used to remove background fields.

Dipole inversion is implemented using iterative least-squares fitting in the image domain with Tikhonov regularization [3], [50], [56]:

$$\underset{\chi}{\operatorname{argmin}} \| M \cdot W_N \big(B_L - B_0 \cdot (d * \chi) \big) \|_2^2 + \alpha \| \chi \|_2^2 \tag{7}$$

where B_L represents the local magnetic field, and α denotes Tikhonov regularization weight. The QSM pipeline is available upon a request from [46].

III. METHODS

A. Validations on a numerical phantom

To assess the efficiency of MP-PCA denoising we generated a numerical phantom using MATLAB software (R2021a, The MathWorks, Natick, MA) which was also used to implement the denoising algorithm.

Phantom was designed as a cylinder aligned along the z-axis (the direction of B_0) filled with four smaller cylindrical tubes with varying magnetic susceptibilities. Each tube's proton density was set to 1 [a.u.]. In order to assess the denoising performance under realistic conditions, simulation parameters were matched to typical experimental parameters using an isotropic resolution of $0.75 \ mm^3$ and $B_0 = 3 \ T$. $\Delta B_0(\vec{r})$ was calculated using the forward model in (5) and depended only on differences in magnetic susceptibility, meaning that phase variations at TE=0, assocaited with RF coils or sample electrical conductivity, were omitted from the simulation. The phase within each voxel was then derived based on:

$$\theta(\vec{r}) = 2\pi \cdot \gamma \cdot (B_0 + \Delta B_0(\vec{r})) \cdot TE \tag{8}$$

Here γ is the hydrogen nucleus gyromagnetic ratio and TE is the echo time.

Next, ΔB_0 and transverse relaxation time constant (T_2) were set for each voxel based on the magnetic susceptibility and relaxivity \mathcal{R} [s⁻¹·mM⁻¹] of Gd-DTPA [57], [58], a common contrast agent used in clinical imaging. T_2' , which corresponds to microscopic field inhomogeneities caused by the susceptibility variations, was calculated as [59]:

$$T_2' = \left(2\pi \cdot \gamma \cdot \Delta B_0(\vec{r})\right)^{-1} \tag{9}$$

The T_2^* value in each voxel was then calculated according to: $1/T_2^* = 1/T_2 + 1/T_2'$.

Lastly, a series of complex T_2^*w images was generated for $N_E = 8$ echo times using standard exponential decay model, with the following TEs: $TE_1 = 3$ ms; $\Delta TE = 4$ ms. Complex white Gaussian noise was added to the series of T_2^* -weighted images using MATLAB's wgn function at SNRs of 10 and 20 with respect to the highest magnitude of the T_2^*w image. This process was repeated 16 times for each SNR level, with different randomized noise patterns to allow gold standard calculation of SNR. Denoising was applied using the MP-PCA pipeline described in Section II above, and a $2 \times 2 \times 2 \times N_E$ window.

In order to estimate the R_2^* relaxation rate of the tissue and its inverse, the T_2^* , we performed an exponential fit of the magnitude signal within each voxel [59]. QSM values were calculated using the QSM pipeline pre- and post-denoising (Tikhonov regularization weight was set to $\alpha=0.05$). After MP-PCA denoising, the coefficient of determination (R^2) was calculated for each voxel as an estimate of the goodness-of-fit of the R_2^* exponential decay model. To prevent bias caused by outliers voxels with $R^2 < 0.8$ were excluded from further calculations of the mean and standard deviation (SD) of R_2^* , and T_2^* (TABLE II). For fair comparison, the same voxels were also excluded from the mean and SD, calculated for the original R_2^* , and T_2^* maps.

SNR maps were calculated for the first echo of T_2^*w , and for quantitative R_2^* , T_2^* maps, and QSM from the 16 repetitions, according to:

$$SNR_{map}(\vec{r}) = \frac{\bar{I}(\vec{r})}{\sigma(\vec{r})}$$
 (10)

where \bar{l} and σ are the mean and SD of the signal in each voxel across all 16 repetitions. The average SNR for each tube for all the maps was estimated based on the mean SNR across all voxels in the tube.

B. Application on healthy volunteers and patients with brain metastases and sickle cell anemia

1) MRI Scans

Four healthy volunteers and four patients were scanned using 3D multi-GRE protocols (see TABLE I for detailed scan parameters). The volunteers and two patients with brain metastases were scanned on a 3T Siemens Prisma scanner. A third patient with sickle cell anemia was scanned on a 1.5T Philips Achieva scanner, and a patient with Parkinson's disease was scanned on a 7T Siemens Magnetom scanner. Informed written and verbal consent were obtained for all participants. Healthy volunteers' scans were approved by the local institutional review board (IRB) committee (approval numbers 3933-17-SMC). Scans of two volunteers with brain metastases were approved by the local ethics committee (IRB approvals TLV-0038-08 and TLV-0200-10), scans of a volunteer with sickle cell anemia were approved by IRB MUHAS-IRB Ref.2014-11-03/EC/Vol.IX/32 and scan of the volunteer with Parkinson's disease was approved by the Queen Square ethics committee, reference 15/LO/00476.

TABLE I SCAN PARAMETERS, MULTI-ECHO 3D-GRE ACQUISITIONS.

State	Scan No.	Voxel size [mm³]	TR [ms]	TE ₁	ΔTE [ms]	No. of Echoes	FA [deg]	Acc.	Scan time [m:s]	
Healthy 1	Scan 1	0.6	45	3.99	5.24	8	15		7:48	
Ticality 1	Scan 2	0.75	43	3.77	3.24	0	13		6:14	
Healthy 2	Scan 3	0.5	68	8.00	8.00	8	15	-	14:09	
nealiny 2	Scan 4	0.5	08	8.00	8.00	0	13	2	7:34	
Healthy 3	Scan 5	0.75	37	2.99	4.25	8	12	2	6:14	
nealiny 3	Scan 6	1	31	4.77	4.23	0	12		3:57	
Healthy 4	Scan 7	0.6	37	2.99	4.25	8	12	2	6:23	
nealiny 4	Scan 8	0.75	31	2.99	4.23	0	12		6:14	
Brain Metastasis	Pt. 1 Pt. 2	0.75	45	3.99	5.24	8	15	2	4:08	
Sickle cell disease	Pt. 3	1.5	27.4	4.28	4.94	5	15	2	4:44	
	Pt. 4 -			2.2			6			
Parkinson's	*******	0.6	19.5		2.38	6		2	9:10	
disease	Pt. 4 - T1w			2.3			24			

Healthy volunteers were also scanned using an MP2RAGE protocol for brain segmentation, with the following parameters: slice thickness = 1 mm, matrix size = 192×156 , field of view = $192 \times 156 mm^2$, TE/TR = 3.52/4000 ms, $N_{slices} = 192$, GRAPPA acceleration factor = 2, total scan time = 6:00 min.

For the patient with Parkinson's disease another QSM pipeline was used. PDw and T1w images underwent identical QSM processing. 3D complex phase data (adaptive combined) were separated into odd and even echo trains before complex (non-linear) echo fitting [49] and phase unwrapping using ROMEO [60]. Two-pass masking was applied [61] The pass 1 mask was generated by thresholding the ROMEO phase-quality map, and this was combined with a BET [54] brain mask of the last echo magnitude to produce the pass 2 mask. Background field removal was completed using projection to dipole fields [55] images were rotated to align with B_0 [62], and dipole inversion used Star-QSM [24] PDw and T1w susceptibility maps were coregsitered and averaged to give the final susceptibility maps [63].

2) Data processing

MP-PCA denoising was applied on T_2^*w complex DICOM images from all scans using a window size of $W = 2 \times 2 \times 2 \times N_E$, followed by generating quantitative R_2^* , T_2^* and QSM maps ($\alpha = 0.05$). For a 256 × 208 × 80 matrix with 8 echoes the denoising step took 242.4 seconds and the QSM processing took 710.1 seconds on a single core Intel Xeon Gold 6150 CPU. MP2RAGE images were segmented and then registered to the multi-echo 3D-GRE image space

using Freesurfer software [64]. Denoising was assessed in three 2D regions of interest (**ROIs**): the globus pallidus, caudate nucleus, and putamen (contralateral regions were analyzed separately). The same R^2 criterion for goodness-of-fit was used here. An single voxel erosion was applied to all ROIs to avoid partial volume effects.

The mean and SD of the T_2^*w images' magnitude, T_2^* values, R_2^* values, and QSM values were estimated in each 2D ROI for a single representative slice. The SNR of the first echo T_2^*w magnitude images was assessed by dividing the mean signal in each ROI by the SD of the signal across four background rectangles similar to [42], [65]. Noise in magnitude images obeys the Rayleigh distribution [66], whereas the denoising process was applied on complex data, where noise is characterized by the Gaussian distribution. To correct for this difference, SD values of background ROIs were divided by the factor $\sqrt{2-\pi/2}$ according to [65].

The proposed denoising technique was compared with two other denoising methods, performed as a preprocessing step for the QSM pipeline. The first method was Gaussian filtering as described in [67], and the second was BM4D denoising, which is based on grouping, transforming, and thresholding of similar 3D patches [68].

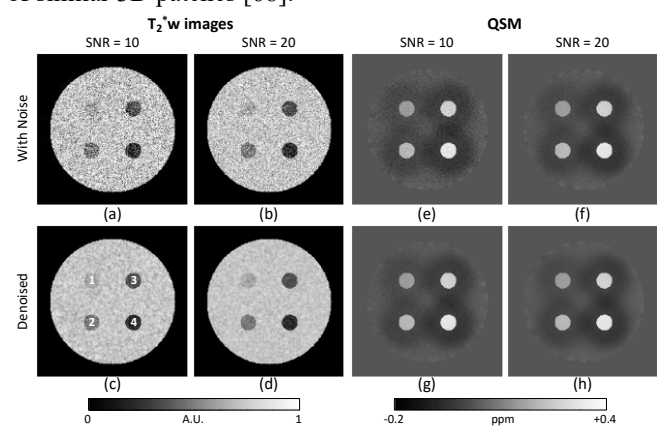


Fig. 2. MP-PCA denoising of a numerical phantom. (a-d) T_2^*w images (4th echo) pre- and post-denoising. (e-h) QSM maps pre- and post-denoising. Simulations were done at SNRs of 10 & 20. Tube numbers are shown in (c).

TABLE II

MEAN, SD, AND SNR OF T_2^*w , R_2^* , T_2^* , and QSM values, calculated for the numerical phantom. SNR values were calculated from 16 repetitions.

	T2*w values (1st echo)									R ₂ * maj	p			T ₂ * map								QSM						
ė	N	Iean [a.	n]	SD	[a.u]	u] SNR		Me	ean [se	n [sec ⁻¹]		SD [sec-1]		SNR		Mean [ms]		SD [ms]		SNR		Mean [ppb]			SD [ms]		SNR	
Tube N	Org.	w/ noise	Den.	w/ noise	Den.	w/ noise	Den.	Org.	w/ noise	Den.	w/ noise	Den.	w/ noise	Den.	Org.	w/ noise	Den.	w/ noise	Den.	w/ noise	Den.	Org.	w/ noise	Den.	w/ noise	Den.	w/ noise	Den.
#1	0.98	0.98	0.98	0.10	0.02	10.5	44.5	7.4	7.7	7.4	3.8	1.0	1.9	7.6	135.5	247.2	137.3	792.0	18.8	1.2	7.4	148.3	148.5	148.5	29.1	18.43	6.7	27.2
#2	0.97	0.97	0.97	0.10	0.02	10.4	44.3	11.2	11.2	11.2	4.4	1.1	2.6	10.8	89.1	117.9	89.8	128.6	8.6	1.8	10.7	208.6	209.1	209.2	32.87	22.71	9.0	36.6
#3	0.96	0.96	0.96	0.10	0.02	10.3	43.8	15.1	14.8	15.1	4.8	1.1	3.2	13.6	66.4	78.2	66.7	57.2	5.1	2.5	13.5	262.4	263.2	263.2	36.69	26.33	10.6	42.7
#4	0.94	0.95	0.95	0.10	0.02	10.2	43.1	18.9	18.6	18.9	5.1	1.2	3.7	15.9	52.9	58.5	53.1	20.9	3.5	3.2	15.8	307.9	309.5	309	40.81	29.47	11.4	45.6

 $No.= number, \ T_2^*w = T_2^* \ weighted, \ Org.= original, \ w/= with, \ Den.= denoised, \ R_2^*w = R_2^* \ weighted, \ ppb=parts \ per \ billion. \ T_2^*w = R_2^* \ weighted, \ ppb=parts \ per \ billion.$

IV. RESULTS

 T_2^*w images and QSM maps of the numerical phantom are illustrated in Fig. 2 for SNRs of 10 and 20 pre- and postdenoising. Fig. 3 shows the corresponding R_2^* , and T_2^* maps. The denoising procedure enhanced the quality of all images and maps, producing more homogeneous structures, which had T_2^*w , T_2^* and R_2^* values closer to ground truth. Quantitative values, corresponding to each tube are detailed in TABLE II. As the simulated noise was generated with zero mean, its addition and removal by denoising did not change the baseline values of the real and imaginary channels of the T_2^*w complex dataset, indicating that no bias was introduced by the denoising process. The SD of the T_2^*w signal magnitude decreased by 76.6 ± 0.0 % post-denoising (averaged across four tubes), associated with an increase of 324.2 ± 1.0 % in SNR. Fitting of R_2^* values produced an error of 0.2 ± 2.4 % pre-denoising, (averaged across four tubes), which decreased to 0.0 ± 0.1 % post-denoising. Similar findings were observed in the SD of R_2^* values, which exhibited an average decrease of 75.4 ± 0.9 % post-denoising, associated with an increase of $321.0 \pm 7.0 \%$ in SNR. Quantitative T_2^* values were overestimated by 35.8 \pm 28.0 % pre-denoising, which was resolved post-denoising, where a negligible deviation of 0.8 ± 0.4 % was observed vs. true T_2^* values. SD of T_2^* values decreased by 91.3 \pm 5.2 % postdenoising, associated with an increase of 459.2 \pm 51.6 % in SNR.

Notably, although T_2^* is the inverse of R_2^* , a drastically different bias emerged between the two types of values. This was reflected in the coefficient of variation (CV) which increased by 72.2 % when moving from R_2^* to T_2^* . This can be attributed to noise propagation during the conversion of R_2^* to T_2^* values, which involves a division operation ($T_2^* = 1/R_2^*$). This changes the noise distribution, leading to a strong overestimation of T_2^* values. This effect was more pronounced for higher T_2^* values, as they correspond to R_2^* values that are closer to zero.

QSM maps demonstrated no bias in mean values both preand post-denoising. We ascribe this stability to the QSM pipeline's reliance on a spatial magnitude weighting matrix W_N , as reported in [20]. As expected, the SD in QSM values was smaller by 30.9 ± 3.5 % post-denoising, corresponding to an increase of 304 ± 3.8 % in SNR. An example of the effect of denoising on the raw signal decay curves is shown in Fig. 4, juxtaposing the original (noisy) and denoised T_2^*w signal values. Denoised signals (red '*') exhibit significantly reduced variability compared to the noisy signals (blue ' \blacksquare '), closely following the original decay curves (green '+'). Efficient denoising was achieved for all three data types and two SNRs without visible loss of information.

 T_2^*w images, T_2^* maps, and QSM maps for a healthy volunteer (scan 8 in TABLE I) are shown in Fig. 5 pre- and post-denoising. The denoising process (~3.66 sec per slice 256 × 208) did not introduce any visible blurring, preserving the fine anatomical details as

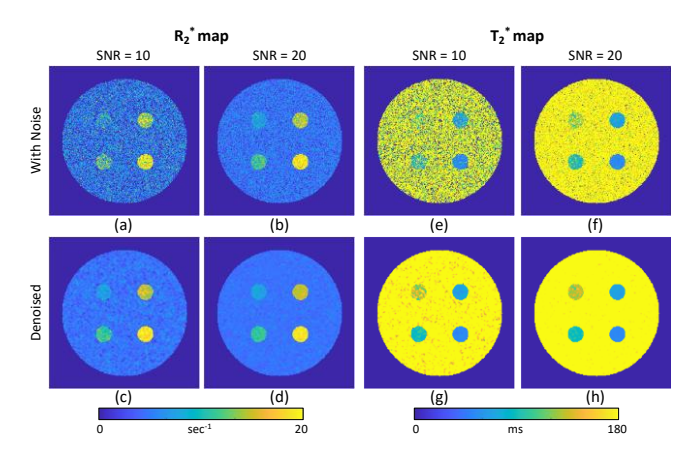


Fig. 3. R_2^* (a-d) and T_2^* (e-h) maps pre- and post- MP-PCA denoising of the numerical phantom at SNRs of 10 & 20.

exemplified by the zoomed-in insets (middle and bottom rows). Quantitative R_2^* , T_2^* , and QSM values are given in TABLE III for each ROI. An average increase of $1.1 \pm 0.6 \%$ in the R_2^* values was observed post-denoising across all ROIs, with a corresponding decrease of 20.3 ± 7.0 % in SD. An average decrease of 2.9 ± 0.9 % in T_2^* values was observed post-denoising, with a corresponding decrease of 23.9 ± 10.2 % in SD. The denoising pipeline did not induce any consistent trend in the QSM values, producing an average change of 0.5 \pm 2.5 % in mean values and an average decrease of 10.8 ± 5.1 % in SD post-denoising. SNR in all assayed ROIs was estimated for T_2^*w images, using four regions in the image background to represent the noise magnitude (see Section III). A consistent increase in the T_2^*w images' SNR was observed for all ROIs with an average improvement of 74.2 \pm 0.2 % post-denoising. SNR values were also calculated for five more scans acquired with different scan parameters. For scan no. 3, an improvement of 139.2 ± 0.4 % post-denoising was observed. For scan no. 4, which had the same acquisition parameters except acceleration factor of factor 2, the denoising process produced a similar improvement of 139.3 \pm 1.3 %. For scans

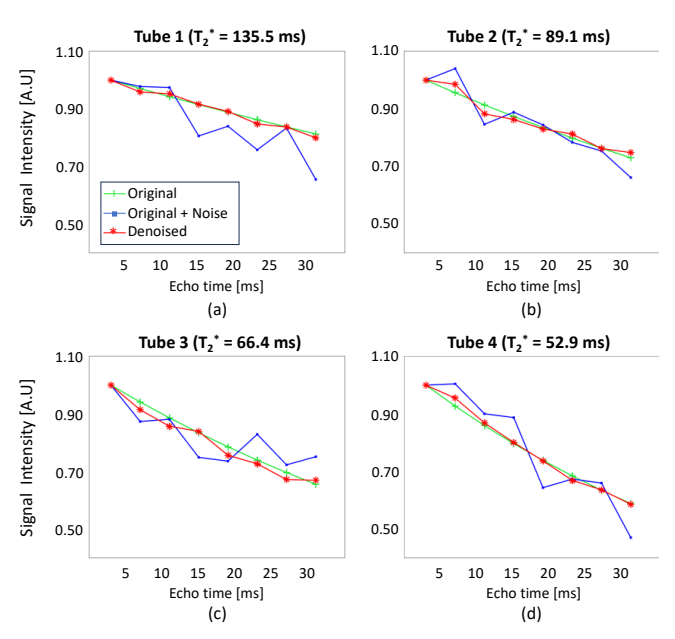


Fig. 4. T_2^* decay curves for all four tubes in the numerical phantom. The green line ('+' marker) denotes the original decay curve, the blue (' \mathbf{n} ' marker) denotes the original decay curve with added noise, and the red line ('*' marker) denotes the denoised signal.

5, 6, and 7 improvements of 179.9 ± 0.8 %, 28.8 ± 0.3 %, and 252.8 ± 2.2 % were seen respectively. These results demonstrate the robustness of MP-PCA denoising across different scan parameters.

Fig. 6 depicts QSM maps for two subjects with brain metastases pre- and post-denoising. Zoomed-in views of the tumors areas demonstrate the preservation of anatomical details of the tissue post-denoising while enhancing the maps' SNR. As described in Section II, the inverse problem in QSM mapping is ill-posed, leading to potential streaking artifacts, an issue highlighted in various previous studies [20], [69]. Fig. 7 demonstrates the utility of MP-PCA denoising for decreasing QSM map artifacts in a patient with sickle cell anemia. The vertical (and horizontal) lines of alternating bright and dark voxels may be caused by pulsatile blood flow. This is significantly reduced by the denoising process, demonstrating its utility in alleviating this type of QSM artifacts.

Fig. 8 present the effect of the denoising algorithm on a volunteer with Parkinson's disease. The scan protocols and the QSM pipeline were different compared to other scans presented in the paper.

Fig. S3-6 presents the effect of different denoising techniques on the T_2^*w images and R_2^* , T_2^* , and QSM maps from Scan 1. As can be seen, the suggested MP-PCA denoising technique and the BM4D technique reduces noise while maintaining fine details, whereas the Gaussian denoising produced smoothing and blurring effects.

V. DISCUSSION

This study evaluated MP-PCA denoising of T_2^*w images and

derived R_2^* , T_2^* and QSM maps. Successful application of the technique was demonstrated in a numerical phantom where both the accuracy and precision of all measured values were increased post-denoising. In vivo validations were also performed in both healthy brains and in the presence of pathologies, demonstrating a proof-of-concept of effective denoising across a range of acquisition parameters, field strengths, acceleration factors, echo times, acquisition bandwidths, and resolutions up to 8 times higher than ones commonly used for QSM. Anatomical details were consistently preserved for all assayed settings with no visible loss of information.

In terms of generalizability, a notable advantage of MP-PCA denoising is that it requires no preliminary assumptions or adjustments of the hardware or scan parameters. In contrast to previous reports [40]–[42], this study showed that effective denoising can be achieved using a relatively small number of echoes. Overall, this allowed acquisitions at sub-millimeter resolutions of up to 0.5 mm³ and low flip angles whilst producing clinically acceptable SNR. MP-PCA denoising was also compared to other commonly-used denoising methods, and produced susceptibility maps preserving far more fine structure. Note that drastically longer processing times were observed for the BM4D method compared to the others, especially for high resolution data.

A. Considerations of MP-PCA denoising

Several factors influence the denoising procedure, ultimately determining the final SNR levels and quantitative values.

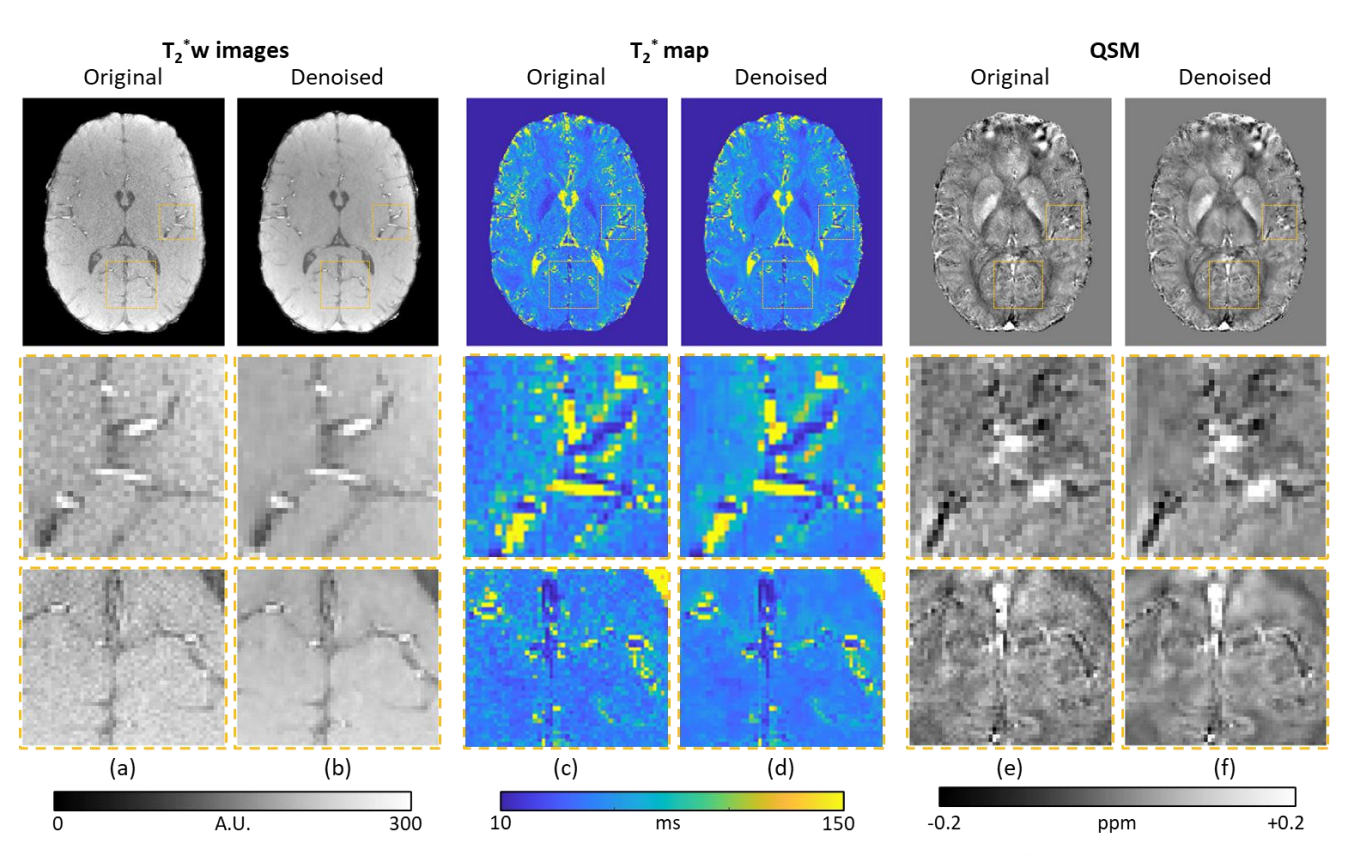


Fig. 5. MP-PCA denoising of brain anatomy of a healthy subject #4 pre- and post-denoising. (a-b) T_2^*w images (first echo), (c-d) T_2^* maps, (e-f) QSM maps pre- and post- denoising. Zoomed regions of interest are shown below each type of image/map (marked by an orange dashed rectangles). Efficient denoising is achieved for all data types without visible loss of information.

TABLE III SNR VALUES FOR T_2^* WEIGHTED IMAGES, ALONGSIDE QUANTITATIVE R_2^* , T_2^* , AND QSM VALUES PRE- AND POST-DENOISING FOR SIX ROIS, SEGMENTED USING FREESURFER FOR A HEALTHY VOLUNTEER.

	R ₂ * map							T ₂ * map							QSM						
	Mean [sec ⁻¹]			SD [sec ⁻¹]			Mean [ms]			SD [ms]			Mo	ean [pp	ob]	SD [ppb]					Diff
	Org.	Den.	Diff. [%]	Org.	Den.	Diff. [%]	Org.	Den.	Diff. [%]	Org.	Den.	Diff. [%]	Org.	Den.	Diff. [%]	Org.	Den.	Diff. [%]	Org.	Den.	Diff. [%]
L. G. Pallidus	35.7	36.2	1.5	8.3	6.5	-21.6	30.0	28.9	-3.7	9.4	7.4	-20.4	107.8	107.2	-0.5	78.5	73.6	-6.3	10.3	18.0	73.9
R. G. Pallidus	37.2	37.7	1.5	8.0	6.6	-17.5	28.3	27.5	-2.8	7.3	6.2	-14.0	143.7	142.4	-0.9	58.3	54.2	-7.1	10.2	17.7	74.1
L. C. Nucleus	20.6	20.7	0.5	4.6	3.5	-24.7	51.1	49.6	-2.9	11.7	7.7	-34.3	53.0	54.3	2.4	40.1	36.0	-10.3	10.3	17.9	74.3
R. C. Nucleus	21.2	21.3	0.1	5.5	5.1	-7.5	50.6	50.0	-1.2	14.8	13.4	-10.0	53.1	51.0	-4.0	27.0	24.3	-10.0	9.7	16.9	74.1
L. Putamen	23.4	23.8	1.7	4.6	3.2	-30.5	44.4	42.7	-3.8	9.3	5.7	-38.0	44.9	46.1	2.8	28.6	22.4	-21.6	10.8	18.8	74.4
R. Putamen	22.5	22.8	1.5	4.5	3.6	-20.0	46.2	44.8	-3.1	9.3	6.8	-27.1	47.9	46.4	-3.0	34.4	31.1	-9.5	10.1	17.7	74.4

ROI=region of interest, L.=left, R.=Right, G. Pallidus=Globus Pallidus, C. Nucleus=Caudate Nucleus, Org.=original, Den.=denoised, Diff.=Difference, SD=standard deviation

First, scanning parameters, mainly spatial-resolution and acquisition bandwidth, will affect SNR. Here, we demonstrated how MP-PCA denoising successfully improved the SNR across various scan parameters and acceleration factors, allowing higher resolutions or bandwidths to be used while still achieving acceptable diagnostic quality.

Since all data were acquired using a 3D multi-GRE protocol, a 3D isotropic moving window was used for all datasets with the number of echoes determining the fourth dimension (see Section II). A minimal window size of $2 \times 2 \times 2$ pixels was found to be optimal for denoising, resulting in a 4D window of $2 \times 2 \times 2 \times N_E$, vectorized to $[N_V \times N_E] = 8 \times N_E$. Since the number of eigenvalues of PCA decomposition is determined by the smallest dimension (minimum of N_V and N_E) [47], and given that multi-GRE protocols are limited to typically 5-10 echoes, choosing a larger window would not have changed the number of PCs and hence might cause a smoothing effect as can be seen in online Figure Sup. 3 [21]. This is similar to Does et al. [41] where a 2D window of $N_W \times N_W$ was used (for a 2D acquisition), where $N_W \approx \sqrt[2]{N_E}$, corresponding to our use of a 3D window size of $N_W \approx \sqrt[3]{N_E}$.

Parallel imaging, such as GRAPPA, is generally recommended for QSM [21], yet can lead to variable noise pattern across the imaged FOV, which may affect the performance of the denoising algorithm. Our findings reveal that despite this potential challenge the MP-PCA denoising performance was not impaired when using moderate R = 2 acceleration. This is described in Section IV, where the relative increase in SNR was similar between accelerated and non-accelerated data (scans 3 and 4).

B. Propagation of noise between R_2^* and T_2^* maps

The addition of noise in the numerical simulation led to an artificial overestimation of T_2^* values compared to ground truth. This was caused due to the non-linear combination of real and imaginary images, altering the noise distribution, a process extensively elaborated in [66]. As reported, for SNR values >3, the noise patterns closely resemble a Gaussian distribution, retaining the original variance (σ^2) but with a mean value adjusted to $sqrt(I_0^2 + \sigma^2)$, where I_0 is the

original magnitude of the signal. As SNR decreases below 3, e.g., at later echo times, the noise distribution shifts to Rician, leading to an even more pronounced elevation of the signal magnitude, as demonstrated by Stern et al. [42]. These effects were mitigated post-denoising, allowing the use of later timepoints which were previously below the noise level. It is important to emphasize that similar to [36], [37], [40], denoising was applied to complex T_2^*w data (magnitude and phase) to maintain the Marchenko-Pastur noise distribution and minimize Rician noise at later echo times. The propagation of noise was further investigated when transitioning from T_2^*w images to R_2^* and T_2^* maps. Analysis showed that pre-denoising, R_2^* values exhibited a small and non-systematic deviation from the original values, unlike the corresponding T_2^* values which demonstrated a significant overestimation. This is likely due to the proximity of R_2^* values to zero, leading to the amplification of noise during the division operation used for calculating T_2^* values. This particularly affected high T_2^* values corresponding to low R_2^* values (see TABLE II). We therefore recommend relying on R_2^* values where possible to minimize augmentation of postprocessing noise.

C. Denoising of QSM data

The variations in the main magnetic field $\Delta B_0(\vec{r})$ are at the core of QSM and are derived from phase images. Previous studies report that the noise at each voxel in the phase image has a Gaussian distribution, while its SD is inversely proportional to the corresponding voxel's magnitude, which, in turn, depends on the local proton density, and $B_1^+/B_1^$ profiles [50], [51]. Throughout the QSM pipeline, this noise propagates through several non-linear operations, which alter its original Gaussian distribution and introduce higher variability among voxels with the same susceptibility (this can be seen in Fig. 2 and TABLE II). MP-PCA denoising reduces the phase noise, thereby mitigating some of the noise amplification induced by the QSM pipeline without loss of information, as demonstrated in Fig. 1 and in TABLE II. The QSM reconstruction implemented in our study followed the pipeline and regularization scheme outlined in [46]. The integration of MP-PCA denoising into

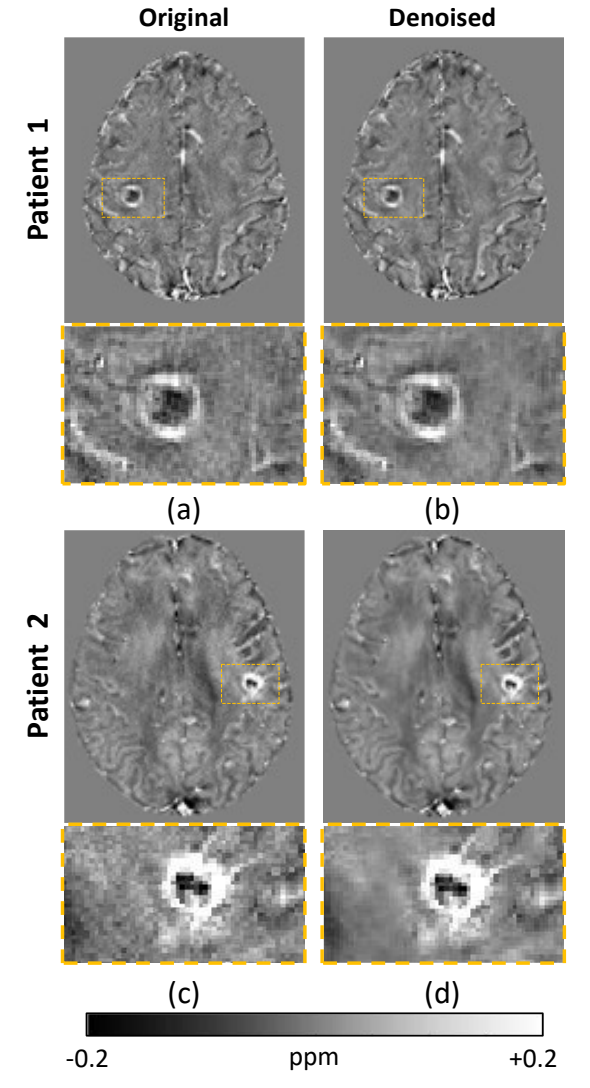


Fig. 6. MP-PCA denoising of QSM maps for two patients with brain metastases located next to the postcentral gyrus **(a-b)**, and next to the precentral gyrus **(c-d)**. Zoomed regions of interest are shown below each map (marked in orange dashed rectangles).

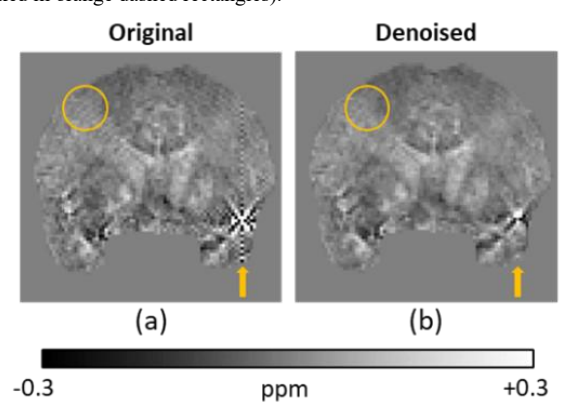


Fig. 7. Utility of MP-PCA denoising for decreasing QSM map artifacts in a patient with sickle cell anemia. The vertical (and horizontal) lines of alternating bright and dark voxels may be caused by pulsatile blood flow. (a) Artifacts in the pre-denoised map, marked with orange arrows. (b) Attenuation of streaking artifact post-denoising around this high-susceptibility region which may contain a blood vessel. The denoising process has also reduced the intensity of repeated edge artifacts which may be due to patient motion, aliasing that was incompletely resolved by parallel imaging, or Gibbs artifacts (orange circle).

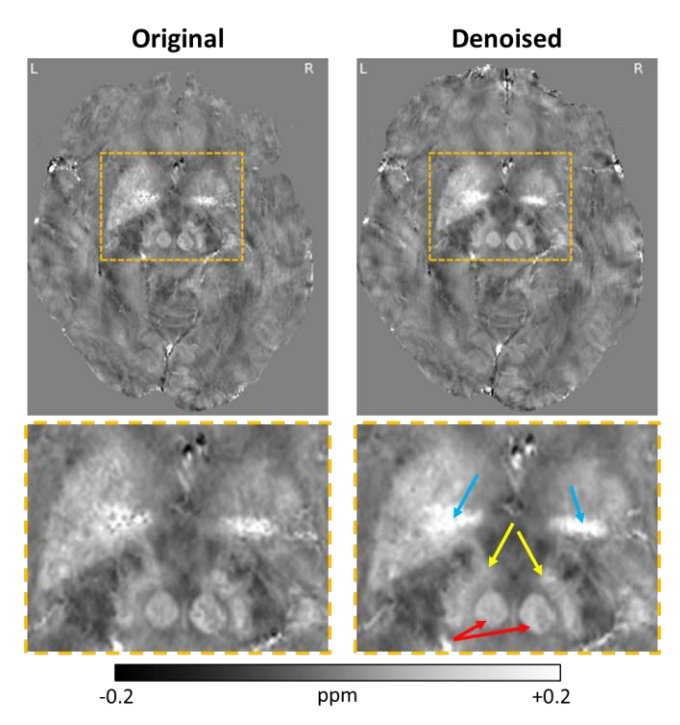


Fig. 8. Axial QSM maps pre- and post-denoising for a patient with Parkinson's disease, showing midbrain structures. Top row presents the full brain slices, with regions of interest highlighted in yellow boxes. The bottom row shows magnified views of these regions. Blue arrows mark the Globus Pallidus, yellow arrows point to the Substantia Nigra, and red arrows mark the Red Nuclei.

other QSM pipelines with different regularization parameters is expected to be similarly effective and remains a prospect for future research. One example is truncated K-space division (TKD) [1], a common method for rapidly obtaining a solution to the inverse problem. The TKD technique is highly sensitive to noise [20] leading to potentially significant artifacts in the susceptibility map, making it an ideal candidate for denoising algorithms. Another example is supervised and unsupervised QSM deep learning reconstruction methods. Many of these methods use the $\Delta B_0(\vec{r})$, which already suffers from propagated noise. The presented technique will allow to reduce the noise effect at this stage for a better input for QSM pipelines. Moreover, as the suggested denoising pipeline is applied prior to QSM, one may assume that other deep learning methods that use the complex image as an input such as [70], can also benefit from better precision and SNR-improved images. The Appendix exemplifies a possible implementation of the denoising process at even earlier stage, i.e., on the images from each coil channel, before coil combination is performed.

QSM is valuable for differentiating intratumoral hemorrhages and calcifications that may result from therapeutic response of metastatic brain tumors. Fig. 6, shows differences between two patients with brain metastases, where the first patient's QSM map contains a lesion with pronounced calcification (potentially indicative of treatment efficacy [71]), while the second exhibits a lesion with a much thicker rim associated with prominent hemorrhagic pathology [72]. This proof-of-concept application provides another example for the ability of MP-PCA denoising to improve the diagnostic quality of QSM in the clinic, allowing more precise comparison between metastases with different origins

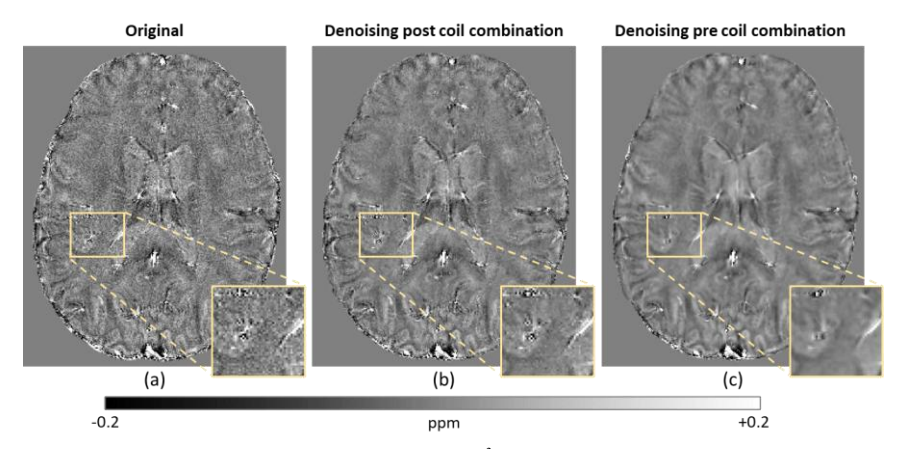


Fig. 9. QSM maps of an In vivo scan 1, and voxel size of an isotropic 0.6 mm^3 . (a) QSM based on the original data. (b) QSM that was derived from the denoising of the complex T_2^*w coil combined data. (c) QSM was derived by denoising each channel of the complex T_2^*w data and then coil combined.

or treatments, and for comparing different time points in longitudinal studies [73].

VI. CONCLUSIONS

The current study highlights the utility of MP-PCA denoising for enhancing the diagnostic quality of QSM maps by improving their SNR and alleviating QSM-specific artifacts, thereby enabling the acquisition of higher resolution data. Recognizing the need for a larger test cohort, these initial results nevertheless provide a sound proof-of-concept for the effectiveness of MP-PCA denoising of T_2^* -weighted images and their quantitative T_2^* , R_2^* and QSM derivatives.

VII. APPENDIX

To assess the impact of different coil combination schemes, MP-PCA denoising was applied on data acquired without acceleration for one healthy volunteer using three different coil combination procedures: adaptive combination done directly on the scanner; adaptive combination done during post-processing based on the method described by Bernstein *et al.* [74]; similar adaptive combination done post-denoising, which was implemented for each of the 16 channels separately.

 T_2^* and QSM maps were compared for each of the three coil combination schemes and shown in Fig. 9. The denoising procedure improved the image quality and QSM quality in all three cases. However, denoising of uncombined complex images from each channel separately yielded the most significant visual enhancements in the QSM maps. A drawback of working with uncombined complex images, however, is the increased processing time due to the need to denoise each channel individually. Another limitation is that uncombined complex images from each coil are typically not available, particularly for retrospective studies. Given these limitations, and following the recommendations in the QSM Consensus paper [21], our study used magnitude and phase DICOM images as inputs.

VIII. ACKNOWLEDGMENTS

We would like to express our sincere gratitude to Patrick Fuchs for his help with the QSM pipeline. RSW is supported by a Wellcome Career Development Award (2025263/Z/22/Z) and has received support from the National

Institute of Health Research UCLH Biomedical Research Centre.

IX. REFERENCES

- [1] K. Shmueli, J. A. De Zwart, P. Van Gelderen, T.-Q. Li, S. J. Dodd, and J. H. Duyn, "Magnetic susceptibility mapping of brain tissue in vivo using MRI phase data," *Magn. Reson. Med.*, vol. 62, no. 6, pp. 1510–1522, Dec. 2009.
- [2] E. M. Haacke, S. Liu, S. Buch, W. Zheng, D. Wu, and Y. Ye, "Quantitative susceptibility mapping: current status and future directions," *Magnetic Resonance Imaging*, vol. 33, no. 1, pp. 1–25, Jan. 2015.
- [3] Y. Wang and T. Liu, "Quantitative susceptibility mapping (QSM): Decoding MRI data for a tissue magnetic biomarker," *Magn. Reson. Med.*, vol. 73, no. 1, pp. 82–101, Jan. 2015.
- [4] K. Shmueli, "Quantitative Susceptibility Mapping," in Advances in Magnetic Resonance Technology and Applications, vol. 1, Elsevier, 2020, pp. 819–838.
- [5] S. Eskreis-Winkler, Y. Zhang, J. Zhang, Z. Liu, A. Dimov, A. Gupta, and Y. Wang, "The clinical utility of QSM: disease diagnosis, medical management, and surgical planning," NMR in Biomedicine, vol. 30, no. 4, p. e3668, Apr. 2017.
- [6] X. Miao, S. Choi, B. Tamrazi, Y. Chai, C. Vu, T. D. Coates, and J. C. Wood, "Increased brain iron deposition in patients with sickle cell disease: an MRI quantitative susceptibility mapping study," *Blood*, vol. 132, no. 15, pp. 1618–1621, Oct. 2018.
- [7] S. Straub, T. M. Schneider, J. Emmerich, M. T. Freitag, C. H. Ziener, H. Schlemmer, M. E. Ladd, and F. B. Laun, "Suitable reference tissues for quantitative susceptibility mapping of the brain," *Magnetic Resonance in Med*, vol. 78, no. 1, pp. 204–214, Jul. 2017.
- [8] S. Straub, F. B. Laun, M. T. Freitag, C. Kölsche, A. Von Deimling, M. Denoix, M. Bendszus, H.-P. Schlemmer, M. E. Ladd, and T. M. Schneider, "Assessment of Melanin Content and its Influence on Susceptibility Contrast in Melanoma Metastases," *Clin Neuroradiol*, vol. 30, no. 3, pp. 607–614, Sep. 2020.
- [9] S. Zeng, H. Ma, D. Xie, Y. Huang, M. Wang, W. Zeng, N. Zhu, Z. Ma, Z. Yang, J. Chu, and J. Zhao, "Quantitative susceptibility mapping evaluation of glioma," *Eur Radiol*, vol. 33, no. 10, pp. 6636–6647, Apr. 2023.
- [10] P. Ravanfar, S. M. Loi, W. T. Syeda, T. E. Van Rheenen, A. I. Bush, P. Desmond, V. L. Cropley, D. J. R. Lane, C. M. Opazo, B. A. Moffat, D. Velakoulis, and C. Pantelis, "Systematic Review: Quantitative Susceptibility Mapping (QSM) of Brain Iron Profile in Neurodegenerative Diseases," Front. Neurosci., vol. 15, p. 618435, Feb. 2021.
- [11] A. Deistung, F. Schweser, and J. R. Reichenbach, "Overview of quantitative susceptibility mapping," NMR in Biomedicine, vol. 30, no. 4, p. e3569, Apr. 2017.
- [12] D. Zhou, J. Cho, J. Zhang, P. Spincemaille, and Y. Wang, "Susceptibility underestimation in a high-susceptibility phantom: Dependence on imaging resolution, magnitude contrast, and other parameters," *Magnetic Resonance in Med*, vol. 78, no. 3, pp. 1080– 1086, Sep. 2017.
- [13] A. Karsa, S. Punwani, and K. Shmueli, "The effect of low resolution and coverage on the accuracy of susceptibility mapping," *Magnetic Resonance in Med*, vol. 81, no. 3, pp. 1833–1848, Mar. 2019.

- [14] A. K. Lotfipour, S. Wharton, S. T. Schwarz, V. Gontu, A. Schäfer, A. M. Peters, R. W. Bowtell, D. P. Auer, P. A. Gowland, and N. P. S. Bajaj, "High resolution magnetic susceptibility mapping of the substantia nigra in Parkinson's disease," *Magnetic Resonance Imaging*, vol. 35, no. 1, pp. 48–55, Jan. 2012.
- [15] E. Y. Kim, Y. H. Sung, H.-G. Shin, Y. Noh, Y. Nam, and J. Lee, "Diagnosis of Early-Stage Idiopathic Parkinson's Disease Using High-Resolution Quantitative Susceptibility Mapping Combined with Histogram Analysis in the Substantia Nigra at 3 T," J Clin Neurol, vol. 14, no. 1, p. 90, 2018.
- [16] A. V. Dimov, A. Gupta, B. H. Kopell, and Y. Wang, "High-resolution QSM for functional and structural depiction of subthalamic nuclei in DBS presurgical mapping," *Journal of Neurosurgery*, vol. 131, no. 2, pp. 360–367, Aug. 2019.
- [17] C. C. Voon, T. Wiltgen, B. Wiestler, S. Schlaeger, and M. Mühlau, "Quantitative susceptibility mapping in multiple sclerosis: A systematic review and meta-analysis," *NeuroImage: Clinical*, vol. 42, p. 103598, 2024.
- [18] M. J. Cronin, S. Wharton, A. Al-Radaideh, C. Constantinescu, N. Evangelou, R. Bowtell, and P. A. Gowland, "A comparison of phase imaging and quantitative susceptibility mapping in the imaging of multiple sclerosis lesions at ultrahigh field," *Magn Reson Mater Phy*, vol. 29, no. 3, pp. 543–557, Jun. 2016.
- [19] M. Marcille, S. Hurtado Rúa, C. Tyshkov, A. Jaywant, J. Comunale, U. W. Kaunzner, N. Nealon, J. S. Perumal, L. Zexter, N. Zinger, O. Bruvik, Y. Wang, E. Sweeney, A. Kuceyeski, T. D. Nguyen, and S. A. Gauthier, "Disease correlates of rim lesions on quantitative susceptibility mapping in multiple sclerosis," *Sci Rep*, vol. 12, no. 1, p. 4411, Mar. 2022.
- [20] S. Wang, T. Liu, W. Chen, P. Spincemaille, C. Wisnieff, A. J. Tsiouris, W. Zhu, C. Pan, L. Zhao, and Y. Wang, "Noise Effects in Various Quantitative Susceptibility Mapping Methods," *IEEE Trans. Biomed. Eng.*, vol. 60, no. 12, pp. 3441–3448, Dec. 2013.
- [21] B. Bilgic, M. Costagli, K.-S. Chan, J. Duyn, C. Langkammer, J. Lee, X. Li, C. Liu, J. P. Marques, C. Milovic, S. D. Robinson, F. Schweser, K. Shmueli, P. Spincemaille, S. Straub, P. van Zijl, Y. Wang, and I. E.-M. T. P. S. Group, "Recommended Implementation of Quantitative Susceptibility Mapping for Clinical Research in The Brain: A Consensus of the ISMRM Electro-Magnetic Tissue Properties Study Group," 2023.
- [22] E. Biondetti, A. Karsa, F. Grussu, M. Battiston, M. C. Yiannakas, D. L. Thomas, and K. Shmueli, "Multi-echo quantitative susceptibility mapping: how to combine echoes for accuracy and precision at 3 Tesla," *Magnetic Resonance in Med*, vol. 88, no. 5, pp. 2101–2116, Nov. 2022.
- [23] E. Biondetti, A. Karsa, D. L. Thomas, and K. Shmueli, "Investigating the accuracy and precision of TE-dependent versus multi-echo QSM using Laplacian-based methods at 3 T," *Magnetic Resonance in Med*, vol. 84, no. 6, pp. 3040–3053, Dec. 2020.
- [24] H. Wei, R. Dibb, Y. Zhou, Y. Sun, J. Xu, N. Wang, and C. Liu, "Streaking artifact reduction for quantitative susceptibility mapping of sources with large dynamic range: Streaking Artifact Reduction for QSM," NMR Biomed., vol. 28, no. 10, pp. 1294–1303, Oct. 2015.
- [25] S. D. Robinson, K. Bredies, D. Khabipova, B. Dymerska, J. P. Marques, and F. Schweser, "An illustrated comparison of processing methods for MR phase imaging and QSM: combining array coil signals and phase unwrapping," NMR in Biomedicine, vol. 30, no. 4, p. e3601, Apr. 2017.
- [26] Y. Ma, E. L. Mazerolle, J. Cho, H. Sun, Y. Wang, and G. B. Pike, "Quantification of brain oxygen extraction fraction using QSM and a hyperoxic challenge," *Magnetic Resonance in Med*, vol. 84, no. 6, pp. 3271–3285, Dec. 2020.
- [27] H. Sun and A. H. Wilman, "Quantitative susceptibility mapping using single-shot echo-planar imaging: Echo-Planar Quantitative Susceptibility Mapping," Magn. Reson. Med., vol. 73, no. 5, pp. 1932–1938, May 2015.
- [28] A. De, H. Sun, D. J. Emery, K. S. Butcher, and A. H. Wilman, "Rapid quantitative susceptibility mapping of intracerebral hemorrhage," *Magnetic Resonance Imaging*, vol. 51, no. 3, pp. 712–718, Mar. 2020.
- [29] P.-L. Bazin, A. Alkemade, W. Van Der Zwaag, M. Caan, M. Mulder, and B. U. Forstmann, "Denoising High-Field Multi-Dimensional MRI With Local Complex PCA," Front. Neurosci., vol. 13, p. 1066, Oct. 2019
- [30] Z. Zhang, J. Cho, L. Wang, C. Liao, H. Shin, X. Cao, J. Lee, J. Xu, T. Zhang, H. Ye, K. Setsompop, H. Liu, and B. Bilgic, "Blip updown acquisition for spin- and gradient-echo imaging (BUDA-SAGE) with self-supervised denoising enables efficient T₂, T₂*, para- and dia-magnetic susceptibility mapping," *Magnetic Resonance in Med*, vol. 88, no. 2, pp. 633–650, Aug. 2022.

- [31] Y. Gao, Z. Xiong, S. Shan, Y. Liu, P. Rong, M. Li, A. H. Wilman, G. B. Pike, F. Liu, and H. Sun, "Plug-and-Play latent feature editing for orientation-adaptive quantitative susceptibility mapping neural networks," *Medical Image Analysis*, vol. 94, p. 103160, May 2024.
- [32] S. Bollmann, K. G. B. Rasmussen, M. Kristensen, R. G. Blendal, L. R. Østergaard, M. Plocharski, K. O'Brien, C. Langkammer, A. Janke, and M. Barth, "DeepQSM using deep learning to solve the dipole inversion for quantitative susceptibility mapping," *NeuroImage*, vol. 195, pp. 373–383, Jul. 2019.
- [33] J. Yoon, E. Gong, I. Chatnuntawech, B. Bilgic, J. Lee, W. Jung, J. Ko, H. Jung, K. Setsompop, G. Zaharchuk, E. Y. Kim, J. Pauly, and J. Lee, "Quantitative susceptibility mapping using deep neural network: QSMnet," *NeuroImage*, vol. 179, pp. 199–206, Oct. 2018.
- [34] Z. Xiong, Y. Gao, Y. Liu, A. Fazlollahi, P. Nestor, F. Liu, and H. Sun, "Quantitative susceptibility mapping through model-based deep image prior (MoDIP)," *NeuroImage*, vol. 291, p. 120583, May 2024.
- [35] Z. Xiong, Y. Gao, F. Liu, and H. Sun, "Affine transformation edited and refined deep neural network for quantitative susceptibility mapping," *NeuroImage*, vol. 267, p. 119842, Feb. 2023.
- [36] Y. C. Eldar, A. O. Hero Iii, L. Deng, J. Fessler, J. Kovacevic, H. V. Poor, and S. Young, "Challenges and Open Problems in Signal Processing: Panel Discussion Summary from ICASSP 2017 [Panel and Forum]," *IEEE Signal Process. Mag.*, vol. 34, no. 6, pp. 8–23, Nov. 2017.
- [37] F. Knoll, K. Hammernik, E. Kobler, T. Pock, M. P. Recht, and D. K. Sodickson, "Assessment of the generalization of learned image reconstruction and the potential for transfer learning," *Magnetic Resonance in Med*, vol. 81, no. 1, pp. 116–128, Jan. 2019.
- [38] QSM Challenge 2.0 Organization Committee, B. Bilgic, C. Langkammer, J. P. Marques, J. Meineke, C. Milovic, and F. Schweser, "QSM reconstruction challenge 2.0: Design and report of results," *Magnetic Resonance in Med*, vol. 86, no. 3, pp. 1241–1255, Sep. 2021.
- [39] V. A. Marčenko and L. A. Pastur, "DISTRIBUTION OF EIGENVALUES FOR SOME SETS OF RANDOM MATRICES," *Math. USSR Sb.*, vol. 1, no. 4, pp. 457–483, Apr. 1967.
- [40] J. Veraart, D. S. Novikov, D. Christiaens, B. Ades-aron, J. Sijbers, and E. Fieremans, "Denoising of diffusion MRI using random matrix theory," *NeuroImage*, vol. 142, pp. 394–406, Nov. 2016.
- [41] M. D. Does, J. L. Olesen, K. D. Harkins, T. Serradas-Duarte, D. F. Gochberg, S. N. Jespersen, and N. Shemesh, "Evaluation of principal component analysis image denoising on multi-exponential MRI relaxometry," *Magnetic Resonance in Med*, vol. 81, no. 6, pp. 3503–3514, Jun. 2019.
- [42] N. Stern, D. Radunsky, T. Blumenfeld-Katzir, Y. Chechik, C. Solomon, and N. Ben-Eliezer, "Mapping of magnetic resonance imaging's transverse relaxation time at low signal-to-noise ratio using Bloch simulations and principal component analysis image denoising," NMR in Biomedicine, vol. 35, no. 12, p. e4807, Dec. 2022.
- [43] F. Grussu, M. Battiston, J. Veraart, T. Schneider, J. Cohen-Adad, T. M. Shepherd, D. C. Alexander, E. Fieremans, D. S. Novikov, and C. A. M. Gandini Wheeler-Kingshott, "Multi-parametric quantitative in vivo spinal cord MRI with unified signal readout and image denoising," *NeuroImage*, vol. 217, p. 116884, Aug. 2020.
- [44] B. Ades-Aron, G. Lemberskiy, J. Veraart, J. Golfinos, E. Fieremans, D. S. Novikov, and T. Shepherd, "Improved Task-based Functional MRI Language Mapping in Patients with Brain Tumors through Marchenko-Pastur Principal Component Analysis Denoising," *Radiology*, vol. 298, no. 2, pp. 365–373, Feb. 2021.
- [45] J. Mosso, D. Simicic, K. Şimşek, R. Kreis, C. Cudalbu, and I. O. Jelescu, "MP-PCA denoising for diffusion MRS data: promises and pitfalls," *NeuroImage*, vol. 263, p. 119634, Nov. 2022.
- [46] A. Karsa, S. Punwani, and K. Shmueli, "An optimized and highly repeatable MRI acquisition and processing pipeline for quantitative susceptibility mapping in the head-and-neck region," *Magnetic Resonance in Med*, vol. 84, no. 6, pp. 3206–3222, Dec. 2020.
- [47] E. R. Henry and J. Hofrichter, "[8] Singular value decomposition: Application to analysis of experimental data," in *Methods in Enzymology*, vol. 210, Elsevier, 1992, pp. 129–192.
- [48] J. V. Manjón, P. Coupé, L. Concha, A. Buades, D. L. Collins, and M. Robles, "Diffusion Weighted Image Denoising Using Overcomplete Local PCA," PLoS ONE, vol. 8, no. 9, p. e73021, Sep. 2013.
- [49] T. Liu, C. Wisnieff, M. Lou, W. Chen, P. Spincemaille, and Y. Wang, "Nonlinear formulation of the magnetic field to source relationship for robust quantitative susceptibility mapping: Robust QSM With Nonlinear Data Fidelity Constraint," *Magn Reson Med*, vol. 69, no. 2, pp. 467–476, Feb. 2013.
- [50] B. Kressler, L. De Rochefort, Tian Liu, P. Spincemaille, Quan Jiang, and Yi Wang, "Nonlinear Regularization for Per Voxel Estimation

- of Magnetic Susceptibility Distributions From MRI Field Maps," *IEEE Trans. Med. Imaging*, vol. 29, no. 2, pp. 273–281, Feb. 2010.
- [51] L. De Rochefort, R. Brown, M. R. Prince, and Y. Wang, "Quantitative MR susceptibility mapping using piece-wise constant regularized inversion of the magnetic field," *Magn. Reson. Med.*, vol. 60, no. 4, pp. 1003–1009, Oct. 2008.
- [52] C. U. MRI Research Lab, "Cornell MRI Research Lab Research Interests." [Online]. Available: https://pre.weill.cornell.edu/mri/pages/qsm.html. [Accessed: 23-Jan-2024].
- [53] F. Schweser, A. Deistung, K. Sommer, and J. R. Reichenbach, "Toward online reconstruction of quantitative susceptibility maps: Superfast dipole inversion," *Magnetic Resonance in Med*, vol. 69, no. 6, pp. 1581–1593, Jun. 2013.
- [54] S. M. Smith, "Fast robust automated brain extraction," *Human Brain Mapping*, vol. 17, no. 3, pp. 143–155, Nov. 2002.
- [55] T. Liu, I. Khalidov, L. De Rochefort, P. Spincemaille, J. Liu, A. J. Tsiouris, and Y. Wang, "A novel background field removal method for MRI using projection onto dipole fields (PDF)," NMR in Biomedicine, vol. 24, no. 9, pp. 1129–1136, Nov. 2011.
- [56] "MRI susceptibility calculation methods, https://xip.uclb.com/product/mri qsm tkd.".
- [57] Y. Shen, F. L. Goerner, J. T. Heverhagen, C. Snyder, D. Hu, X. Li, and V. M. Runge, "In vitro T2 relaxivities of the Gd-based contrast agents (GBCAs) in human blood at 1.5 and 3 T," *Acta Radiol*, vol. 60, no. 6, pp. 694–701, Jun. 2019.
- [58] N. M. Hijnen, A. Elevelt, J. Pikkemaat, C. Bos, L. W. Bartels, and H. Grüll, "The magnetic susceptibility effect of gadolinium-based contrast agents on PRFS-based MR thermometry during thermal interventions," *J Ther Ultrasound*, vol. 1, no. 1, p. 8, Dec. 2013.
- [59] G. B. Chavhan, P. S. Babyn, B. Thomas, M. M. Shroff, and E. M. Haacke, "Principles, Techniques, and Applications of T2*-based MR Imaging and Its Special Applications," *RadioGraphics*, vol. 29, no. 5, pp. 1433–1449, Sep. 2009.
- [60] B. Dymerska, K. Eckstein, B. Bachrata, B. Siow, S. Trattnig, K. Shmueli, and S. D. Robinson, "Phase unwrapping with a rapid opensource minimum spanning tree algorithm (ROMEO)," *Magnetic Resonance in Med*, vol. 85, no. 4, pp. 2294–2308, Apr. 2021.
- [61] A. Karsa and K. Shmueli, "A New, Simple Two-Pass Masking Approach for Streaking Artifact Removal in Any QSM Pipeline," presented at the ISMRM, 2022.
- [62] O. C. Kiersnowski, A. Karsa, S. J. Wastling, J. S. Thornton, and K. Shmueli, "Investigating the effect of oblique image acquisition on the accuracy of QSM and a robust tilt correction method," *Magnetic Resonance in Med*, vol. 89, no. 5, pp. 1791–1808, May 2023.
- [63] R. Murdoch, Kawadler, Carmichael, Kirkham, and Shmueli, "Can Multi-Parametric Mapping Sequences Be Used for Accurate Quantitative Susceptibility Mapping?," presented at the ISMRM, 2020.
- [64] B. Fischl, "FreeSurfer," NeuroImage, vol. 62, no. 2, pp. 774–781, Aug. 2012.
- [65] F. L. Goerner and G. D. Clarke, "Measuring signal-to-noise ratio in partially parallel imaging MRI," *Medical Physics*, vol. 38, no. 9, pp. 5049–5057, Sep. 2011.
- [66] H. Gudbjartsson and S. Patz, "The rician distribution of noisy mri data," Magn. Reson. Med., vol. 34, no. 6, pp. 910–914, Dec. 1995.
- [67] J. Chen, B. Ades-Aron, H.-H. Lee, S. Mehrin, M. Pang, D. S. Novikov, J. Veraart, and E. Fieremans, "Optimization and validation of the DESIGNER preprocessing pipeline for clinical diffusion MRI in white matter aging," *Imaging Neuroscience*, vol. 2, pp. 1–17, Apr. 2024.
- [68] M. Maggioni, V. Katkovnik, K. Egiazarian, and A. Foi, "Nonlocal Transform-Domain Filter for Volumetric Data Denoising and Reconstruction," *IEEE Trans. on Image Process.*, vol. 22, no. 1, pp. 119–133, Jan. 2013.
- [69] F. Schweser, K. Sommer, A. Deistung, and J. R. Reichenbach, "Quantitative susceptibility mapping for investigating subtle susceptibility variations in the human brain," *NeuroImage*, vol. 62, no. 3, pp. 2083–2100, Sep. 2012.
- [70] Y. Gao, Z. Xiong, A. Fazlollahi, P. J. Nestor, V. Vegh, F. Nasrallah, C. Winter, G. B. Pike, S. Crozier, F. Liu, and H. Sun, "Instant tissue field and magnetic susceptibility mapping from MRI raw phase using Laplacian enhanced deep neural networks," *NeuroImage*, vol. 259, p. 119410, Oct. 2022.
- [71] T. Harada, K. Kudo, N. Fujima, M. Yoshikawa, Y. Ikebe, R. Sato, T. Shirai, Y. Bito, I. Uwano, and M. Miyata, "Quantitative Susceptibility Mapping: Basic Methods and Clinical Applications," *RadioGraphics*, vol. 42, no. 4, pp. 1161–1176, Jul. 2022.

- [72] W. Chen, W. Zhu, Ii. Kovanlikaya, A. Kovanlikaya, T. Liu, S. Wang, C. Salustri, and Y. Wang, "Intracranial Calcifications and Hemorrhages: Characterization with Quantitative Susceptibility Mapping," *Radiology*, vol. 270, no. 2, pp. 496–505, Feb. 2014.
- [73] H. Jiang, Z. Li, Y. Sun, J. Ren, F. Yan, Q. Sun, H. Wei, and L. Bian, "Irreversible Alterations of Susceptibility in Cushing's Disease: A Longitudinal QSM Study," *The Journal of Clinical Endocrinology & Metabolism*, vol. 108, no. 8, pp. 2007–2015, Jul. 2023.
- [74] M. A. Bernstein, M. Grgic, T. J. Brosnan, and N. J. Pelc, "Reconstructions of phase contrast, phased array multicoil data," *Magnetic Resonance in Med*, vol. 32, no. 3, pp. 330–334, Sep. 1994.